Coexistence of ferromagnetism and unconventional spin-glass freezing in the site-disordered kagome ferrite SrSn_{2}Fe_{4}O_{11}

L. Shlyk, S. Strobel, B. Farmer, L. E. De Long, and R. Niewa

Phys. Rev. B **97**, 054426 — Published 23 February 2018

DOI: 10.1103/PhysRevB.97.054426

Coexistence of Ferromagnetism and Unconventional Spin Glass Freezing in the Site-Disordered Kagome Ferrite $SrSn_2Fe_4O_{11}$

L. Shlyk[1], S. Strobel[1], B. Farmer[2], L. E. De Long[2*], and R. Niewa[1]

[1] *Institut für Anorganische Chemie, Universität Stuttgart, 70569 Stuttgart, Germany*

[2] *University of Kentucky, Department of Physics and Astronomy, CP177, 505 Rose Street, Lexington KY, USA 40506-0055*

Abstract

Single-crystal x-ray diffraction refinements indicate $SrSn_2Fe_4O_{11}$ crystallizes in the hexagonal *R*-type ferrite structure with non-centrosymmetric space group $P6_3mc$ and lattice parameters a = 5.9541(2) Å, c = 13.5761(5) Å, Z = 2 (R(F) = 0.034). Octahedrally coordinated 2*a* (*M*(1) and *M*(1a)) and 6*c* sites (*M*(2)) have random, mixed occupation by Sn and Fe; whereas the tetrahedrally coordinated 2*b* sites (Fe(3) and Fe(3a)) are exclusively occupied by Fe, whose displacement from the ideal position with trigonal-bipyramidal coordination causes the loss of inversion symmetry. Our dc and ac magnetization data indicate $SrSn_2Fe_4O_{11}$ single crystals undergo ferro- or ferri-magnetic (FM) behavior below a transition temperature T_C = 630 K with very low coercive fields $\mu_o H_{c\perp}$ = 0.27 Oe and $\mu_o H_{c||}$ = 1.5 Oe at 300 K, for applied field perpendicular and parallel to the ***c***-axis, respectively. The value for T_C is exceptionally high, and the coercive fields exceptionally low, among the known R-type ferrites. Time-dependent dc magnetization and frequency-dependent ac magnetization data indicate the onset of short-range, spin glass freezing below T_f = 35.8 K, which results from crystallographic disorder of magnetic Fe^{3+} and nonmagnetic Sn^{4+} ions on a frustrated Kagome sublattice. Anomalous ac susceptibility and thermomagnetic relaxation behavior in the short-range-ordered state differs from that of conventional spin glasses. Optical measurements in the ultraviolet to visible frequency range in a diffuse reflectance geometry indicate an overall optical band gap at 0.8 eV, consistent with observed semiconducting properties.

KEY WORDS: R-type Ferrites, Kagome Net, Magnetic Relaxation, Spin Glasses, Frustration, Ferromagnetic Semiconductors.

*** Corresponding Author:** lance.delong@uky.edu

1. Introduction

The *R*-type ferrite (RTF) family of ternary oxides includes a range of compositions $(Ba,Sr)M_{2\pm x}M'_{4\mp x}O_{11}$ (M = Mn, Fe, Co, Ni, Cu, Zn; M' = Ru, Ti) **[1-8]** that exhibit a spectrum of fundamental condensed matter physics phenomena. This broad stability range of known RTF compositions retains only one basic hexagonal structure type that features edge-connected $M(2)O_6$ octahedra that form Kagome layers that are prone to magnetic frustration (**Fig. 1**). In spite of their structural and compositional similarities, members of the $(Ba,Sr)M_{2\pm x}Ru_{4\mp x}O_{11}$ subfamily of ruthenates exhibit a remarkable variety of electrical transport and magnetic properties that can be tuned by chemical substitution among 3*d* and 4*d* transition elements, or by simply varying the relative concentration of the 3*d* elements and 4*d* Ru within established homogeneity ranges **[1,2]**.

Atomic disorder has profound effects on the behavior of RTF. On the one hand, the metallic compounds $BaZnRu_5O_{11}$ and $BaNiRu_5O_{11}$ form highly ordered Kagome planes of Ru moments that resist any transition to magnetic order at temperatures below 1 K **[5-7]**. On the other hand, Fe-bearing RTF exhibit atomically disordered Kagome planes and long-range, collinear ferrimagnetic order below remarkably high Curie temperatures (e.g., $T_C \sim 490$ K) **[1,3,4]**.

It is indeed noteworthy that the room-temperature resistivities of the Ba- and Sr-based Fe RTF lie in the range of typical narrow-gap semiconductors (0.001 – 100 Ωcm), and are accompanied by high carrier concentrations and practical carrier mobilities **[1]**. These characteristics make them promising candidates for spin-based, multifunctional materials since they can optimize spin injection and detection efficiencies across a doped-semiconductor/ferromagnetic semiconductor interface. Moreover, the magnetic 3*d* and 4*d* ions of these compounds tend to populate distinct sublattices, which differs from dilute magnetic semiconductors such as (Ga,Mn)As and (Zn,Co)O, which suffer from electrical and magnetic inhomogeneities due to clustering of dilute 3*d* dopants among randomly occupied sites **[9]**. Further, a very large room-temperature anomalous Hall effect (AHE) with a transverse resistivity

ρ_{xy} = 77 μΩ-cm has been observed for $BaFe_{3.4}Ru_{2.6}O_{11}$, which makes this material very attractive for Hall sensor applications **[10]**.

In contrast, the Mn- or Co-bearing Ru ferrites are bad metals with temperature- and field-dependent, non-collinear magnetic structures **[1-4]**. The AHE of these compounds is enhanced above the values expected for a conventional ferromagnet by virtue of a coupling between conduction electrons and a non-trivial spin texture on the Kagome sublattice. The spin chirality of non-collinear spin textures in the presence of geometrical frustration introduces a Berry phase in the itinerant electron states, which leads to an anomalous Hall effect of topological origin (THE) **[3,11,12,13]**. A THE controlled by spin chirality is of great current interest in condensed matter physics, not only for its fundamental scientific importance, but also because of its potential applications in semiconductor spintronics.

Atomic disorder can strongly influence the physical properties of magnetically frustrated lattices **[5,14-16]**. We have investigated the magnetic properties of $SrSn_2Fe_4O_{11}$ as an RTF with relatively strong magnetic interactions among atomically disordered sites, which results in a high ordering temperature. The influence of spin-orbit interactions is also not expected to be decisive in this *3d*-electron material, which should produce distinct differences from the complex behaviors observed for 4*d* (e.g., Ru) and 5*d* (e.g., Ir) oxides **[17]**.

Although $SrSn_2Fe_4O_{11}$ was first synthesized by Cadee and Ijdo **[18]** in 1984, little is known about this material beyond Sn Mössbauer spectroscopy data that characterize local environments in polycrystalline samples **[19]**. As previously found for the Ba-isotypes **[18]**, RTF generally crystallize in a hexagonal structure that is typically identified as the centro-symmetric $P6_3/mmc$ space group, which contains a Kagome substructure formed by edge-sharing $M(2)O_6$ octahedra located within the ***ab*-**plane (**Fig. 1**). These Kagome planes are connected along [001] by face-sharing $M(1)O_6$ octahedra and $M(3)O_5$ trigonal bipyramids. There is a mixing of magnetic 3*d* and 4*d* ions on the *M*(1) and *M*(2) crystallographic sites, while 3*d* elements exclusively occupy the trigonal-bipyramidal-coordinated *M*(3) positions (**Fig. 2**). Note that the Ru 4*d* ions have been

completely replaced with non-magnetic Sn or magnetic Fe ions in the isostructural $SrSn_2Fe_4O_{11}$ compound. Therefore, atomic disorder in $SrSn_2Fe_4O_{11}$ stems from the random distribution of magnetic $Fe^{3+}$and nonmagnetic Sn^{4+} within both the Kagome substructure, and inside the face-sharing $M(1)O_6$ octahedra. This spatial distribution of strongly magnetic Fe^{3+} results in an inhomogeneous local environment for individual spins.

Our x-ray crystal structure refinements of $SrSn_2Fe_4O_{11}$ indicate the Fe^{3+} ions randomly occupy 84% of the *M*(2) sites within the Kagome planes, but occupy only 30 % of the (*M*(1) and *M*(1a)) sites located in face-sharing octahedra connecting adjacent Kagome planes. Although the *M*(3) sites in the bipyramids are exclusively occupied by Fe^{3+}, the higher degree of substitution of nonmagnetic Sn^{4+} for magnetic Fe^{3+} ions in *M*(1) sites located between the Kagome planes should weaken the interlayer coupling and reduce the effective dimensionality of the magnetic lattice, which could alter the cooperative behavior of the compound. Previously, it was shown that magnetic dilution, even at low level, has a significant impact on geometrically frustrated systems with antiferromagnetic nearest-neighbor interactions such as $SrGa_{12-x}Cr_xO_{19}$ ($0 \le x < 1$), whose spin glass transition temperature is strongly reduced with increasing Ga content **[16]**. On the other hand, a study of spin freezing in the diluted spin-ice compounds $Dy_{2-x}Y_xTi_2O_7$ ($0 \le x \le 0.4$), where ferromagnetic interactions are frustrated on the pyrochlore lattice, suggests that their freezing temperature is essentially unchanged by dilution **[14]**. These results indicate different mechanisms of glassy behavior exist in frustrated, site-disordered magnets.

In this work we have investigated the magnetic properties of single crystals of the site-disordered Kagome compound $SrSn_2Fe_4O_{11}$ using dc and ac magnetization measurements. Our results contain evidence of a complex magnetic ground state in which long-range FM order (existing below T_C = 630 K) coexists with a short-range spin glass state below 36 K. The short-range-ordered state exhibits anomalous behavior of the ac susceptibility and thermomagnetic relaxation data which differ from those of conventional spin glasses.

2. Experimental Details

To realize single-crystal growth of $SrSn_2Fe_4O_{11}$, initial amounts of 2.9 mmol SnO_2, 3.1 mmol Fe_2O_3 and 3.2 mmol $SrCl_2$ were mixed and then pressed into a pellet that was heated to 1330^o C and kept at this temperature for several days; the furnace was then slowly cooled to room temperature. Black hexagonal platelets of maximum size 1.5 mm with thicknesses 0.07-0.08 mm were obtained. Small hexagonal platelets were selected for x-ray diffraction at ambient temperature using a 4-circle diffractometer (NONIUS-κ-CCD, Bruker AXS GmbH) with monochromatic MoK_α radiation. An absorption correction based on symmetry-equivalent reflections was applied (program X-SHAPE). The structure was solved using direct methods, and refined (program SHELXS-97-2, SHELXL-97-2 **[20]**), yielding a composition $SrSn_{1.89(5)}Fe_{4.11}O_{11}$. Oxygen atoms were restricted to isotropic displacement parameters in the refinements, due to a limited number of unique intensity data. Details of the data collection and results of the structural refinements are collected in **Tables 1** and **2**; additional information regarding the crystal structure investigations may be obtained from **[21]**.

Chemical microprobe analyses yielded very consistent compositions for all crystals investigated, with inferred atomic density ratios n(Sr)/n(Sn)/n(Fe) = 0.9±0.2 : 2.0±0.1 : 4.0±0.1 (the oxygen content could not be quantified with this technique), in excellent agreement with the composition inferred from x-ray diffraction data, and with no additional elements detected. The x-ray refinement and microprobe results indicate the crystals examined were single phase and of excellent quality.

The magnetization data for separate, oriented single crystals were acquired over a temperature range 1.8 K ≤ T ≤ 300 K in applied magnetic fields 0 ≤ $\mu_o H$ ≤ 5 T using a Quantum Design MPMS7 SQUID Magnetometer. AC magnetic susceptibility data were taken using a 5.0 Oe RMS drive applied in the hexagonal basal plane.

Diffuse reflectance spectra were measured on a J&M TIDAS UV-vis-NIR Spectrophotometer equipped with a reflection measuring head. $BaSO_4$ was used as a white standard. The Kubelka-

Munk function was applied to convert reflectance into absorbance and obtain electronic band gap information.

3. Results and Discussion

Crystal Structure and Composition

There has been considerable work done on the structure of $BaSn_2Fe_4O_{11}$, which was originally described in the hexagonal space group $P6_3/mmc$ from powder neutron diffraction at ambient temperatures [18]. Shortly thereafter, Sn–Fe ordering within the Kagome net was proposed, resulting in orthorhombic symmetry with space group *Cmcm* (direct subgroup of $P6_3/mmc$), based on powder neutron diffraction data acquired at 10 K and 240 K [22-24]. However, later studies carried out on single crystals grown from $BaCl_2/B_2O_3$ flux indicated a hexagonal symmetry was the correct choice [25]. Finally, diffraction experiments using synchrotron radiation performed on microcrystalline powder gave no indication for any deviation from hexagonal symmetry [26]. However, the single-crystal XRD results, together with Mössbauer spectroscopic studies, indicate the Fe/Sn occupation for both octahedrally coordinated metal sites has some dependence on thermal history (i. e., preparation conditions) [19]. Mössbauer spectroscopy also revealed a preference for Fe to be located in tetrahedral rather than trigonal bipyramidal coordination, with 50 % probability for each of the two tetrahedral sites [18].

We have determined that $SrSn_2Fe_4O_{11}$ crystallizes in the hexagonal RTF structure consisting of layers of edge-sharing $M(2)O_6$ octahedra interconnected by face-sharing double octahedra $O_3M(1)O_3M(1a)O_3$ and trigonal bipyramids $Fe(3)O_5$. Our crystal structure refinement for $SrSn_2Fe_4O_{11}$ was first carried out in the centrosymmetric space group $P6_3/mmc$; however, a strong elongation for displacements of Sr in the [001] direction was obtained, proximate to the expected elongation of Fe located in trigonal bipyramidal coordination (Fe(3)). This led us to consider a refinement in the non-centrosymmetric structure $P6_3mc$, which is known to be the

correct space group assignment for the ambient temperature modifications of PbV_6O_{11} and SrV_6O_{11} [27,28], and BaV_6O_{11} below 250 K [29]. The *M*(2) metal sites themselves lie on a nearly ideal Kagome net randomly occupied by 84 % Fe and 16 % Sn with only small distortions and interatomic metal–metal distances slightly below 3 Å. Selected interatomic distances are gathered in **Table 3**. The centers of the double octahedra have mixed occupation by Sn and Fe with a slight excess of Sn (54(2) % Sn, 46 % Fe), while the trigonal bipyramid is centered exclusively by Fe. The lack of centrosymmetry leads to slight displacements of most atoms along [001] and lifts the equivalency of the two metal sites in the face-sharing double octahedra---one being occupied to a larger extent by Sn (*M*(1), 86 %) than the second (*M*(1a), 54 %). Additionally, the two face-sharing tetrahedra that form the trigonal-bipyramidal void are occupied to a different extent---the Fe(3) site to only 19 %, whereas the Fe(3a) site to about 81 %. The displacement of Fe(3a) corresponds to a shift of about 0.2 Å along the [001] direction with respect to the ideal center position in the trigonal bipyramidal void. The *M*(1) and *M*(1a) sites are significantly displaced from the ideal position at the octahedra centers towards the terminal faces of the edge-sharing $O_3M(1)O_3M(1a)O_3$ double octahedra, due to Coulomb repulsion between the positive metal ions.

The only crystal structure data for $SrSn_2Fe_4O_{11}$ in the current literature are **1)** unit cell parameters obtained from powder samples [18], which are in good agreement with our values (*a* = 5.9558(9) Å, *c* = 13.5429(21) Å versus *a* = 5.9541(2) Å, *c* = 13.5761(5) Å); and **2)** an analysis of Sn and Fe distribution over the three possible sites in $P6_3/mmc$ symmetry obtained from Mössbauer spectroscopy [19] on a sample quenched from 1423 K (no Sn in trigonal coordination, 28 % Sn in face-sharing octahedra and 72 % Sn in Kagome nets). This analysis of site occupancies in $BaSn_2Fe_4O_{11}$ differs from our structure refinements; however, it is important to note that the Mössbauer sample was annealed at 1423 K. In this regard, we note that the distributions of Ti and Fe over these two distinct octahedrally coordinated positions also invert in $BaTi_2Fe_4O_{11}$ if it is annealed at 973 K [19].

Static Magnetic Properties

Figure 3 shows the temperature dependence of the field-cooled (FC) magnetic susceptibility of a $SrSn_2Fe_4O_{11}$ single crystal measured in a 0.1 T magnetic field applied either parallel or perpendicular to the ***c***-axis. All investigated samples undergo a FM phase transition at T_C = 630 K to an ordered state with a finite spontaneous magnetization. The observed Curie temperature is significantly higher than that of other RTF (Ba,Sr)$M_{2\pm x}M'_{4\mp x}O_{11}$ (M = Mn, Fe, Co; M' = Ru, Ti) **[1-6]**. To our knowledge, $SrSn_2Fe_4O_{11}$ has the highest T_C reported among all known members of the RTF family. It should be noted that a much lower T_C = 180 K was reported **[18]** for isostructural $BaSn_2Fe_4O_{11}$, which may be related to differences in the ionic size between Ba^{2+} and Sr^{2+} and/or to a strong influence of the preparation procedure on the cation distribution in $BaSn_2Fe_4O_{11}$ **[19,23-26]**.

Upon further cooling, the DC susceptibility exhibits an anomaly for applied field in both crystallographic directions at T_f = 35.8 K (inset in **Fig. 4**). There is a distinct irreversibility between the ZFC and FC magnetization below T_f, which is a typical signature of the metastable magnetic state commonly found in short-range-ordered materials such as spin glasses **[15]**. Note that our sample presents two essential microscopic ingredients of spin glass freezing----that is, Fe^{3+}/Sn^{4+} site disorder and a geometrically frustrated Kagome lattice. Structural disorder due to the random replacement of magnetic Fe^{3+} by nonmagnetic Sn^{4+} on the Kagome net of $SrSn_2Fe_4O_{11}$ may cause an additional "reentrant spin glass" transition at temperatures below either a long-range ferromagnetic or antiferromagnetic transition **[30-32]**. The high-temperature, long-range-ordered state is frustrated due to the increasing strength of random ferromagnetic or antiferromagnetic interactions with decreasing temperature; consequently, a reentrant spin glass transition occurs with further cooling. However, the divergence between the ZFC and FC magnetizations cannot unambiguously prove the onset of a spin glass state, since this behavior might also be attributed to irreversible domain wall dynamics within the ferromagnetic state, which are reflected in field-dependent, isothermal magnetization data.

Indeed, the dc magnetic hysteresis loops of $SrSn_2Fe_4O_{11}$ exhibit unusual behavior, as shown in **Figs. 5** and **6** for T = 4.5 and 300 K, respectively, and two crystallographic orientations. At room temperature, m(*H*) exhibits weak anisotropy and varies almost linearly with magnetic field above 1.2 T. The low-temperature behavior of m*(H)* is similar for T = 4.5 K, except for its relatively large overall magnitude. The magnetic moment m as a function of $\mu_0 H$ at T = 4.5 K (50 K) yields coercive field values $\mu_o H_{C\perp}$ = 200 Oe (20 Oe) and $\mu_o H_{C||}$ = 270 Oe (25 Oe). Very small coercive fields $\mu_o H_{c\perp}$ = 0.27 Oe and $\mu_o H_{c||}$ = 1.5 Oe are observed for T = 300 K, classifying this material as an extremely soft magnet. The value $\mu_o H_{c\perp}$ = 0.27 Oe is, to our knowledge, the lowest value of coercive field ever reported for ferrites, and is smaller than the coercive fields of $Ni_{0.8}Fe_{0.2}$ (permalloy) thin films, a material widely used in technological applications. Materials dominated by 3*d* magnetism tend to have low magnetic anisotropy and often exhibit soft magnetic behavior. However, the coincidence of such very small coercive fields with non-saturating magnetization, which we observe for $T << T_C$, is unusual.

The temperature dependence of the coercive field of $SrSn_2Fe_4O_{11}$ is shown in **Fig. 4**. The coercivity of $SrSn_2Fe_4O_{11}$ appears to decrease exponentially with temperature, similar to that observed for the frustrated cluster glass Dy_5Pd_2 **[33]**. However, fits of $H_C(T)$ to a simple exponential behavior failed; nevertheless, an expression that includes two activation mechanisms (reflected in two characteristic temperature scales, T_1 and T_2), did provide a satisfactory fit (dashed line in **Fig. 4**):

$$H_C(T) = H_{CO} + H_{C1} \exp(-T / T_1) + H_{C2} \exp(-T / T_2). \qquad \textbf{(1)}$$

The best-fit parameters appropriate to **Fig. 4** are H_{CO} = 5.057 Oe, H_{C1} = 391.2 Oe, T_1 = 4.600 K, H_{C2} = 58.09 Oe, and T_2 = 37.86 K.

Exponential dependences of $H_C(T)$ are not universal in spin glasses; for example the following power law has also been predicted and observed for isotropic spin glasses **[34]**:

$$H_C(T) \propto (1 - T / T_f)^{1/2} \qquad \textbf{(2)}$$

A rapid increase of m(H) with increasing H at low fields, followed by a nearly linear variation of m(H) for $\mu_o H > 1.1$ T, and the failure of m(H) to saturate at high fields, are typical of either a canted antiferromagnetic or ferrimagnetic state **[3,8,13,35]**. Geometrical frustration within the Kagome plane can be accompanied by spin canting along (001) **[3,13]**, induced by antisymmetric Dzyaloshinsky-Moriya (DM) interactions **[36,37]** appropriate for spins in the non-centrosymmetric structure of $SrSn_2Fe_4O_{11}$. Non-zero spin canting gives rise to finite scalar spin chirality and an anomalous Hall effect of topological origin, as observed in the related RTF, $BaMn_{2.49}Ru_{3.51}O_{11}$ **[3]**. Additional neutron diffraction studies of powders and/or larger single crystals are needed to determine the mechanism of the anomalous behavior of m*(H)*.

Previous studies of the $(Sr,Ba)(Fe,Ru)_6O_{11}$ RTF systems indicate that the ratio of the number of 3*d* and 4*d* magnetic ions plays an important role in determining the magnetic anisotropy **[1,2]**: A higher Ru/Fe ratio correlates with higher anisotropy **[1]**, which originates from spin-orbit interactions and an incompletely quenched orbital angular momentum of the relatively large 4*d* orbitals **[17]**. Moreover, the strong decrease in magnetic anisotropy observed for larger substitutions of 3*d* Fe for 4*d* Ru suggests that an increasing Fe/Ru ratio reduces the spin-orbit interaction responsible for the anisotropy **[1]**. Therefore, it is reasonable to associate the very soft magnetic behavior observed in $SrSn_2Fe_4O_{11}$ with a complete substitution of Ru^{3+}/Ru^{5+} by Fe^{3+} and nonmagnetic Sn^{4+}.

Dynamic Magnetic Properties

To obtain further evidence of a spin glass state below 36 K, the dynamic properties of $SrSn_2Fe_4O_{11}$ were investigated by ac susceptibility measurements at low temperatures. **Figure 7** shows the temperature dependence of the ac susceptibility taken in zero dc applied magnetic field. As temperature decreases, the real part of the ac susceptibility, $\chi'(T)$, exhibits a pronounced kink at $T = T_k = 35$ K, which is often used to define the freezing temperature T_f in spin glasses; and an observable frequency dependence of T_k usually signals a transition into a true spin glass state **[15]**. On the other hand, the magnitude of χ' decreases as frequency increases (**Fig. 7a**),

and for temperatures above and well below T_k, the $\chi'(T)$ curves for different frequencies remain separated. Furthermore, the $\chi'(T)$ curves converge to a nonzero, frequency-independent value in the zero-temperature limit, which is a behavior often seen in spin glass materials **[38,39]**. In contrast, the imaginary part of the ac susceptibility, $\chi''(T)$, exhibits a well-defined peak at $T = T_p$ for each frequency investigated (**Fig. 7b**); this peak increases in magnitude, broadens and shifts upward by as much as 20 K on increasing the frequency from 0.1 Hz to 1000 Hz, which is also typical of spin glasses **[15,40-42]**.

A careful comparison of **Figs. 7a** and **7b** reveals an inflection point in $\chi'(T)$ at $T = T_i$, which is well below the kink temperature T_k, but lies slightly below, and tracks the temperature of the peak in χ"(T) at T_p, as shown in **Fig. 8.** Therefore, we will use the more robust peak in χ"(T) to estimate the spin glass freezing point T_f in the following discussion. The magnitude of the frequency dependence of $\chi''(T)$, quantified by $p \equiv \{\Delta T_f/T_f\}\Delta(\log f) \approx 0.12$, is much higher than that of canonical spin glasses (e.g., p = 0.01 **[15]**), but is an order of magnitude lower than that of superparamagnets (e.g., $p \approx 3$ **[15]**), and is comparable to values observed for dilute dipole glasses **[42]** and geometrically frustrated magnets (e.g., $p \approx 0.18$ **[43]**).

The onset of a broad temperature interval with strong frequency dependence distinctly below an initial peak in $\chi'(T)$ which has no frequency dependence, resembles the ac susceptibility data for the reentrant spin glass $Fe_{0.62}Mn_{0.38}TiO_3$ **[44]**. On the other hand, $\chi'(T)$ for $Fe_{0.62}Mn_{0.38}TiO_3$ exhibits no frequency dependence near and well above the kink temperature, which differs from the $\chi'(T)$ data shown for $SrSn_2Fe_4O_{11}$ in **Fig. 7a**. The overall behavior of the ac susceptibility, including a large frequency shift in the peak in $\chi''(T)$ resembles that of a spin-glass like state. In contrast, the absence of a frequency dependence of the kink in $\chi'(T)$, accompanied by a strong frequency-dependence across a wide temperature interval surrounding the kink, indicate that the frozen spin state in $SrFe_2Sn_4O_{11}$ differs from that of conventional spin glass materials.

A change in the sign of χ'' from positive to negative with decreasing temperture $T \leq 8$ K is seen in **Fig. 7b** for frequency $f =$ 1000 Hz, and can be extrapolated from the 700 Hz data. We mention his curious behavior because it violates simple linear response theory (where χ'' is a measure of energy dissipation in the sample); and a negative $\chi''(T)$ has also been observed in the $Na_{0.85}CoO_2$ cobaltate **[45]**, and in the $BiFeO_3$ ferrite, where it was attributed to a modulated magnetic structure **[38]**. Such a sign change has not been reported previously for RTF materials; verification/clarification of this phenomenon will require more detailed magnetothermal measurements at variable frequency.

To clarify the low-temperature dynamics of the spin glass state of $SrFe_2Sn_4O_{11}$, we first applied a simple Arrhenius law to describe the frequency dependence of $T_p \equiv T_f$, as has been done for conventional spin glasses composed of isolated clusters (superparamagnets), where

$$f = f_0 \exp(-E_a/k_B T_f) \qquad (3)$$

Here, E_a and f_0 are the energy barrier and characteristic frequency of a superparamagnet, respectively. The temperatures of the peaks observed in $\chi''(T)$ appear to follow such an Arrhenius law with parameters $E_a/k_B = 138$ K and $\log_{10}(f_0) = 6.7134$, corresponding to $f_0 = 5.169 \times 10^6$ Hz only for $T > 20$ K (see **Fig. 9**). Below 20 K, a clear deviation from the Arrhenius law is observed. Application of a Vogel-Fulcher law $f = f_0 \exp(E_a/k_B(T_f - T_0))$, proposed for magnetically interacting clusters, does not significantly improve the fits.

We tentatively concluded that a non-thermal relaxation process is active in $SrSn_2Fe_4O_{11}$ below about 20 K, recalling the quantum spin relaxations observed in the dilute Ising spin system $LiHo_{1-x}Y_xF_4$ **[40]** and the geometrically frustrated spin-ice $D_2Ti_2O_7$ **[46]**. We therefore measured the frequency dependence of the ac susceptibility of $SrSn_2Fe_4O_{11}$ at various temperatures below $T_f \approx 36$ K, and found $\chi''(f)$ indeed exhibits a double-peak structure (see **Fig. 10**) that indicates the presence of multiple relaxation processes. A double-peak structure was previously found in the ***temperature dependence*** of χ'' of $Fe_{0.62}Mn_{0.38}TiO_3$ **[44]**, where it was attributed to the competition between the weakening of long-range antiferromagnetic order and

growth of a reentrant spin glass phase with decreasing temperature. Double-peaks in the ***frequency dependence*** of χ'' are rarely reported or discussed in the literature, and could reflect the existence of two different types of dynamics driven by thermally activated, or quantum relaxation processes. The higher-frequency peaks clearly show a decrease in the peak frequency as temperature decreases from 31 to 25 K, as expected for thermally-induced spin relaxation. In contrast, additional lower-frequency peaks can be identified at approximately the same frequency (≈ 10 Hz) in the temperature range, $T \geq 22$ K, as expected for quantum spin relaxation. When the temperature is decreased below 25 K, magnetic relaxation becomes very slow, and the position of the dominant peak shifts to lower frequencies. Apparently, the peak structure is gradually transformed as the temperature is lowered, and only a single broad peak is visible at 20 K.

Based on our preliminary analyses of the frequency-dependent ac susceptibility, we conclude that the magnetic dynamics of $SrSn_2Fe_4O_{11}$ are not well described by either the exponential or power law behaviors that are typical for canonical spin glass materials. The mechanism underlying two-peak behavior of $\chi''(f)$ is not clear at present, and detailed investigations of the magnetic structure and dynamics are required to clarify these issues.

A typical signature of complex spin dynamics in spin glasses is a time-dependent magnetization below T_f. We therefore measured the thermomagnetic relaxation of a $SrSn_2Fe_4O_{11}$ sample that was initially field-cooled to 25 K in an applied field H_{FC} = 500 Oe, which was then removed. The magnetization was then measured as a function of time after waiting a certain time t_w. The results for a waiting time t_w = 1000 s are presented in **Fig. 11**. Thermomagnetic magnetization data are typically analyzed using a stretched exponential form based on a phenomenological description of relaxation in disordered systems **[47]**:

$$M(t) = M_0 \exp(-(t/\tau)^{1-n}) \qquad (4)$$

Here, $M_0 = M\ (t = 0)$ and τ is the relaxation time. However, fits to **Eq. 4** yielded very poor results (see dashed line in **Fig. 11**). Alternatively, we attempted to fit the data to a logarithmic

dependence used to describe relaxation processes in systems with long-range magnetic order **[41]**:

$$M(t) = M_0 - C\ln(t) \quad \textbf{(5)}$$

Here M_0 is the initial value of the remanent magnetization and C is a constant that depends on the field, temperature and material. Fits using **Eq. 5** were also unsuccessful.

A closer inspection of the data set revealed two regimes with different time responses: A rapid initial magnetization relaxation is followed by a slower relaxation for t > 1500 s. For times shorter than 1500 s, we find a power-law behavior predicted by Ulrich et *al*. **[48]** (see dotted line in **Fig. 11**):

$$M(t) = M_0\, t^{-\gamma} \quad \textbf{(6)}$$

Here, M_0 is related to the intrinsic ferromagnetic component and γ depends on the strength of magnetic interactions. If the measurements are extended for longer times (t > 1500 s), a crossover from the power-law behavior to a stretched exponential decay, $M(t) = M_0 \exp(-(t/\tau)^n)$, is observed. Indeed, the solid line in **Fig. 11** shows that the thermomagnetic relaxation data are well described by a supersposition of the power-law and stretched exponential forms:

$$M(t) = M_0 t^{-\gamma} + M_1(\exp(-t/\tau)^{1-n}) \quad \textbf{(7)}$$

The best-fit parameters are $M_0 = 6.8 \times 10^{-3}$ emu/mol, $\gamma = 0.18$, $M_1 = 2.6 \times 10^{-2}$ emu/mol, $\tau = 255$ s, and $n = 0.1$.

To summarize our analyses of magnetic dynamics, two processes with different characteristic relaxation times are present in $SrSn_2Fe_4O_{11}$, and they merge into a complex relaxation process below 35 K. Possible relaxation processes include the non-exponential relaxation of dynamically correlated ferromagnetic domains **[48]**, while the stretched exponential form might reflect glassy dynamics of a disordered spin structure inside domains **[47]**.

Optical Measurements

Previous work [1,2] has shown that the long-range magnetic ordering temperatures of various RTF are strongly correlated with the size of the semiconducting gap in the case of non-metallic materials, whereas the ordering temperatures are typically near or below 200 K for metallic examples. We therefore measured the diffuse reflectance spectra of $SrSn_2Fe_4O_{11}$ over the ultraviolet-to-visible frequency range to obtain estimates of the optical band gap. The diffuse reflectance was converted into absorption using the Kubelka-Munk approximation [49,50], which relates the absorption coefficient (α) to the diffusion coefficient (S) of the compound. Three steep absorption thresholds appear in the energy range 0.7 − 3 eV (1750 − 410 nm) (**Fig. 12**). The absorption edge energies (E_g), derived from the intersection point of the base line along the energy axis and the extrapolated line of the linear part of the threshold, exhibit values of approximately 0.8 eV, 1.3 eV and 1.9 eV. We assume that the absorption edge at 0.8 eV can be assigned to the overall optical band gap of the sample as a transition from the valence band to the conduction band, whereas the other two edges observed at 1.3 and 1.9 eV can be assigned to different types of transitions, such as charge transfer or d-d transitions [51-53]. Ligand-to-metal charge transfer (LMCT) from oxide anions towards Fe^{3+} cations can be generally presumed for such transition metal oxides; however, d-d interactions may occur due to crystal field splitting of the 3d orbitals in combination with non-centrosymmetric local environment of the Fe^{3+} ions. The optical thresholds clearly imply that $SrSn_2Fe_4O_{11}$ is a semiconductor, and are consistent with a striking empirical correlation between the magnitudes of the semiconducting gaps and the magnetic ordering temperatures of non-metallic, Fe/Ru-bearing RTF [1].

Conclusion

We have found that single crystals of the $SrSn_2Fe_4O_{11}$ RTF are semiconducting, and exhibit long-range FM order well above room temperature (i.e., T_C = 630 K), accompanied by very low coercive fields $\mu_o H_{C\perp}$ = 0.27 Oe and $\mu_o H_{C||}$ = 1.5 Oe at 300 K. Overall, our measurements of static magnetic properties show $SrSn_2Fe_4O_{11}$ exhibits features typical of long-range FM order,

such as finite remanence, and coercivity that decreases exponentially with increasing temperature. These properties make this material attractive for microwave devices and recording media.

Our lower temperature data and analyses provide strong evidence that the magnetic ground state of $SrSn_2Fe_4O_{11}$ is heterogeneous, due to an apparent coexistence of long-range FM order and an unconventional spin glass state. Low-temperature magnetic measurements on $SrSn_2Fe_4O_{11}$ single crystals reveal a distinct spin-glass anomaly at $T_f = 35.8$ K, which is very far below the onset temperature of long-range magnetic order at $T_C = 630$ K. The spin glass state in $SrSn_2Fe_4O_{11}$ exhibits two regimes of spin glass freezing. One regime is analogous to the dynamic freezing associated with relaxation over a wide range of length and time scales, as in conventional disordered systems, while the second regime is predominantly associated with a single relaxation mode, as observed, for example, in geometrically frustrated systems. We relate the first mode to the large-scale Fe^{3+}/Sn^{4+} site disorder present in $SrSn_2Fe_4O_{11}$, while the second mode is a consequence of the geometrical frustration of the Kagome lattice. $SrSn_2Fe_4O_{11}$ may represent an interesting class of quantum dynamics in a ferromagnet; and further experiments are needed to clarify the nature of the low-temperature spin glass state, especially the double-peak structure of $\chi''(f)$. The coexistence of long-range and unconventional short-range magnetic orders is unusual, and has been previously observed in only a limited number of materials, including geometrically frustrated magnets (see **[54]**, and references therein). The appearance of such a complex ground state is consistent with a competition between the inherent topological frustration of the Kagome network and atomic disorder among the Fe^{3+}/Sn^{4+} sites of $SrSn_2Fe_4O_{11}$.

Acknowledgements

We would like to thank Dr. Falk Lissner for collecting the X-ray diffraction data and Klaus Wolff for the EDX measurements. Research at the University of Kentucky was supported by U.S. National Science Foundation Grant DMR-1506979.

References

1. L. Shlyk, S. Kryukov, B. Schüpp-Niewa, R. Niewa, and L. E. De Long, "High Temperature Ferromagnetism and Tunable Semiconductivity of (Ba,Sr)$M_{2\pm x}Ru_{4\mp x}O_{11}$ (M = Fe, Co): A New Paradigm for Spintronics", Adv. Mater. **20**, 1315 (2008).
2. L. Shlyk, S. Kryukov, B. Schüpp-Niewa, R. Niewa, and L. E. De Long, "Structural, magnetic and transport properties of a novel class of ferromagnetic semiconductors: $SrM_{2\pm x}Ru_{2\pm x}O_{11}$ (M = Fe, Co)", J. Appl. Phys. **103**, 07D112 (2008).
3. L. Shlyk, S. Parkin, and L. E. De Long, "Successive magnetic transitions of the Kagome plane and field-driven chirality in single-crystal $BaMn_{2.49}Ru_{3.51}O_{11}$", Phys. Rev. B **81**, 014413 (2010).
4. L. Shlyk, B. G. Ueland, J. W. Lynn, Q. Huang, L. E. De Long, and S. Parkin, "Magnetic structure, magnetization, and magnetotransport properties of (Ba,Sr)$M_{2\pm x}T_{4\pm x}O_{11}$ (M = Fe, Co; T = Ru, Ti)", Phys. Rev. B **81**, 184415 (2010).
5. L. Shlyk, L. E. De Long and R. Niewa, "Structure and Physical Properties of $SrNiRu_5O_{11}$ Single Crystals: A New R-Type Ferrite with Ordered Kagome Nets", Phys. Rev. B **95**, 024433 (2017). DOI: 10.1103/PhysRevB.95.024433
6. L. Shlyk, S. Strobel, E. Rose and R. Niewa, "$BaZnRu_5O_{11}$: Novel compound with frustrated magnetic lattice based on a distorted Kagome network", Solid State Sciences **14**, 281-286 (2012).
7. Larysa Shlyk, Sabine Strobel, Thomas Schleid and Rainer Niewa, "Ruthenate-ferrites $AMRu_5O_{11}$ (A = Sr, Ba; M = Ni, Zn): Distortion of Kagome nets via metal–metal bonding", Z. Kristallogr. **227**, 545–551 (2012). DOI: 10.1524/zkri.2012.1450
8. M. L. Foo, Q. Huang, J. W. Lynn, W.-L. Lee, T. Klimczuk, I. S. Hagemann, N. P. Ong, R. J. Cava, "Synthesis, structure and physical properties of Ru ferrites: $BaMRu_5O_{11}$ (M = Li and Cu) and $BaM'_2Ru_4O_{11}$ (M' = Mn, Fe and Co)", J. Solid State Chem.**179**, 563-572 (2006).
9. T. Dietl, J. Appl. Phys. **103**, 07D111 (2008).

10. L. Shlyk, R. Niewa, and L. E. De Long, "Anomalous Hall effect in the high-temperature ferrimagnetic semiconductors $BaFe_{2\pm x}Ru_{4\pm x}O_{11}$", Phys. Rev. B **82**,134432 (2010).

11. Y. Taguchi, Y.Oohara, H. Yoshizawa, N. Nagaosa, and Y. Tokura, "Spin Chirality, Berry Phase, and Anomalous Hall Effect in a Frustrated Ferromagnet", Science **291**, 2573 (2001).

12. K. Ohgushi, S. Murakami, and N. Nagaosa, "Spin anisotropy and quantum Hall effect in the Kagome lattice: Chiral spin state based on a ferromagnet", Phys. Rev. B **62**, R6065 (2000).

13. D. Grohol, K. Matan, J.-H. Cho, S.-H. Lee, J. W. Lynn, D. G. Nocera, and Y. S. Lee, "Spin chirality on a two-dimensional frustrated lattice", Nature Materials, **4**, 323 (2005).

14. J. Snyder, J. S. Slusky, R. J. Cava, P. Schiffer, "Dirty spin ice: The effect of dilution on spin freezing in $Dy_2Ti_2O_7$", Phys. Rev. B **66**, 064432 (2002).

15. J. A. Mydosh, Spin Glasses - An Experimental Introduction (Taylor and Francis, London, 1993), pp.98-100, 64-76.

16. B. Martinez, F. Sandiumenge, A. Rouco, A. Labarta, J. Rodriguez-Carvajal, M. Tovar, M. T. Causa, S. Gali, X. Obradors, "Magnetic dilution in the strongly frustrated Kagome antiferromagnet $SrGa_{12-x}Cr_xO_{19}$", Phys. Rev. B **46**, 10786 (1992).

17. G. Cao and L. E. De Long, Eds., *Frontiers of 4d- and 5d-Transition Metal Oxides* (Singapore, World Scientific Publishing, 2013; ISBN 978-981-4374-85-9).

18. M. C. Cadee and D. J. W. Ijdo, "Refinements of the Six-Layer Structures of the R-Type Hexagonal Ferrites $BaTi_2Fe_4O_{11}$ and $BaSn_2Fe_40_{11}$", J. Solid State Chem. **52**, 302 (1984).

19. G. K. Thompson and B. J. Evans, "Structure-property relationships in the R-type hexaferrites: Cation distributions and magnetic susceptibilities of $MX_2Fe_4O_{11}$", Hyperfine Inter. **94**, 2039 (1994).

20. G. M. Sheldrick, SHELXS-97-2, SHELXL-97-2, Universität Göttingen, Göttingen, Germany, 1997.

21. Additional information regarding the crystal structure investigations may be obtained from Fachinformationszentrum Karlsruhe, 76344 Eggenstein-Leopoldshafen, Germany (fax: +49-

7247-808-666; e-mail: crysdata@fiz-karlsruhe.de, http://www.fiz-informationsdienste.de/en/DB/icsd/depot_anforderung.html) on quoting the deposition number CSD-433008.

22. T. Maeda, M. Arihara, M. Kawasaki, S. Sekimoto, M. Shiojiri, J. Electron Microscopy **34,** 214 (1985).

23. I. Sosnowska, R. Przeniosło, M. Shiojiri, P. Fischer, "Neutron-diffraction studies of the crystal and magnetic structure of $BaSn_2Fe_4O_{11}$", Physica B **213&214**, 227 (1995).

24. M. Shiojiri, T. Maeda, T. Isshiki, Y. Hirota, S. Sekimoto, Y. Ikeda, K. Iwauchi, "Crystal Structures and Magnetic Properties of $BaTi_{2-x},Sn_xFe_4O_{11}$", phys. stat. sol. (a) **97**, 231 (1986).

25. M. Drofenik, D. Hanžel, D. Hanžel, M. N. Deschizeaux-Chéruy, J. C. Joubert, "Crystal Growth and Properties of $BaSn_2Fe_4O_{11}$", J. Solid State Chem. **79**, 115 (1989).

26. R. Przeniosło, I. Sosnowska, P. Fischer, T. Wroblewski, M. Shiojiri, "Determination of the Fe/Sn atoms distribution in $BaSn_2Fe_4O_{11}$ by neutron and synchrotron radiation diffraction", Physica B **234-236**, 931 (1997).

27. O. Mentre, F. Abraham, "New Mixed Valence Compounds in the Pb–V–O System: Synthesis and Crystal Structure of Hollandite-Related $Pb_{1.32}V_{8.35}O_{16.7}$ and R-Type Hexagonal Ferrite PbV_6O_{11}", J. Solid State Chem. **125**, 91 (1996).

28. Y. Hata, Y. Kanke, H. Suzuki, G. Kido, J. Appl. Phys. **85**, 4768 (1999).

29. K. Friese, Y. Kanke, "Structural phase transitions in BaV_6O_{11}", J. Solid State Chem. **179**, 3277 (2006).

30. I. A. Campbell, S, Senoussi, F. Varrel, J. Teillet, and A. Hamzic, "Competing Ferromagnetic and Spin-Glass Order in a *Au*Fe Alloy", Phys. Rev. Lett. **50**, 1615 (1983).

31. K. Jonason, J. Mattsson, and P. Nordblad, "Chaos in the Ferromagnetic Phase of a Reentrant Ferromagnet", Phys. Rev. Lett. **77**, 2562 (1996).

32. J. Mattsson, T. Jonsson, P. Nordblad, H. A. Katon, and A. Ito, "No Phase Transition in a Magnetic Field in the Ising Spin Glass $Fe_{0.5}Mn_{0.5}TiO_3$", Phys. Rev. Lett. **74**, 4305 (1995).

33. T. Paramanik, T. Samanta, R. Ranganathan, and I. Das, "Magnetic and magnetocaloric properties of Dy_5Pd_2: role of magnetic irreversibility," RSC Adv., vol. 5, no. 59, pp. 47860–47865, 2015.

34. K. Binder, A. P. Young, "Spin glasses: Experimental facts, theoretical concepts, and open questions", Rev. Mod. Phys. 58, 801 (1986).

35. R. L. Carlin, *Magnetochemistry* (Springer-Verlag, Berlin, 1986).

36. I. Dzyaloshinsky, "A THERMODYNAMIC THEORY OF "WEAK" FERROMAGNETISM OF ANTIFERROMAGNETICS", J. Phys. Chem. Solids **4**, 241 (1958).

37. T. Moriya, Phys. Rev. **120**, 91 (1960).

38. M. K. Singh, W. Prellier, M. P. Singh, R. S. Katiyar, J. F. Scott, "Spin-glass transition in single-crystal $BiFeO_3$", Phys. Rev. B **77**, 144403 (2008).

39. R. Mathieu, D. Akahoshi, A. Asamitsu, Y. Tomioka, Y. Tokura, "Colossal Magnetoresistance without Phase Separation: Disorder-Induced Spin Glass State and Nanometer Scale Orbital-Charge Correlation in Half Doped Manganites", Phys. Rev. Lett. **93**, 227202 (2004).

40. D. H. Reich, T. F. Rosenbaum, G. Aeppli, "Glassy Relaxation without Freezing in a Random Dipolar-Coupled Ising Magnet", Phys. Rev. Lett. **59**, 1969 (1987).

41. P. J. Ford, "Spin Glasses", Contemp. Phys. 23, 141 (1982).

42. J. A. Quilliam, S. Meng, C. G. A. Mugford, J. B. Kycia, "Evidence of Spin Glass Dynamics in Dilute $LiHo_xY_{1-x}F_4$", Phys. Rev. Lett. **101**, 187204 (2008).

43. J. Snyder, J. S. Slusky, R. J. Cava, P. Schiffer, "How `spin ice' freezes", Nature **413**, 48-51 (2001).

44. K. Gunnarsson, P. Svedlindh, J. O. Andersson, P. Nordblad, L. Lundgren, H. Aruga Katori, A. Ito, "Magnetic behavior of a reentrant Ising spin glass", Phys. Rev B **46**, 8227 (1992).

45. J.–S. Rhyee, J. B. Peng, C. T. Lin, S. M. Lee, "Anisotropic magnetization and dynamic susceptibility sign change in single-crystal $Na_{0.85}Co_2$", Phys. Rev. B **77**, 205108 (2008).

46. J. Snyder, B. G. Ueland, J. S. Slusky, H. Karunadasa, R. J. Cava, P. Schiffer, "Low-temperature spin freezing in the $Dy_2Ti_2O_7$ spin ice", Phys. Rev. B **69**, 064414 (2004).

47. G. Williams, D. C. Watts, "Non-Symmetrical Dielectric Relaxation Behaviour Arising from a Simple Empirical Decay Function", Trans. Far. Soc. **66**, 80 (1970).

48. M. Ulrich, J. Garca-Otero, J. Rivas, A. Bandeet, "Slow relaxation in ferromagnetic nanoparticles: Indication of spin-glass behavior", Phys. Rev. B **67**, 024416 (2003).

49. Kotum, G. *Reflectance Spectroscopy*; Springer-Verlag: New York, 1969.

50. Wendlandt, W. W.; Hecht, H. G. *Reflectance Spectroscopy*; Interscience Publishers: New York, 1966.

51. Hwang, D. W.; Kim, H.G.; Lee, J. S.; Kim, J.; Li, W.; Oh, H., „Photocatalytic Hydrogen Production from Water over M-Doped $La_2Ti_2O_7$ (M = Cr, Fe) under Visible Light Irradiation ($\lambda > 420$ nm)", J. Phys. Chem. B **109**, 2093-2102 (2005).

52. Sherman, D. M.; Vergo, N., „Optical (diffuse reflectance) and Miissbauer spectroscopic study of nontronite and related Fe-bearing smectites", *American Mineralogis*t **73**, 1346-1354 (1988).

53. Sherman, D. M., „Electronic spectra of Fe3+ oxides and oxide hydroxidesin the near IR to near UV", *American Mineralogis*t **70**, 1262-1269 (1985).

54. J. E. Greedan, „Geometrically frustrated magnetic materials", J. Mater. Chem. **11**, 37 (2001).

Table 1. Crystal structure data for $SrSn_2Fe_4O_{11}$.

Formula	$SrSn_{1.89(5)}Fe_{4.11}O_{11}$
Crystal system	hexagonal
Space group	$P6_3mc$
a, Å	5.9541(2)
c, Å	13.5761(5)
V, Å^3	416.8
Z	2
D_{calcd}, g cm^{-3}	5.77
μ(MoK_α), mm^{-1}	19.1
F(000), e	660
hkl range	±7,±7, ±18
$2\theta_{max}$, deg	56.22
Refl. measured	6574
Refl. unique	428
R_{int}	0.077
Param. refined	41
R(F)/wR(F^2) (all reflections)	0.034/0.070
GoF (F^2)	1.196
BASF[a)]	0.47(4)
$\Delta\rho_{fin}$ (max/min), e Å^{-3}	0.76

[a)] inversion twinning of single crystals

Table 2. Crystal structure parameters of $SrSn_2Fe_4O_{11}$.

Atom	Site	*x*	*y*	*z*	U_{eq} / Å^2
Sr	2*b*	1/3	2/3	0.2487(5)	0.0163(7)
M(1)*	2*a*	0	0	0.14349(8)	0.009(1)
M(1a)*	2*a*	0	0	0.3575(1)	0.003(1)
M(2)*	6*c*	0.5003(2)	0.0006(4)	0.0001(5)	0.0065(4)
Fe(3)*	2*b*	2/3	1/3	0.222(3)	0.008(1)
Fe(3a)*	2*b*	2/3	1/3	0.2620(5)	U_{eq}(Fe(3))
O(1)$^+$	6*c*	0.172(1)	2 *x*	0.0797(7)	0.009(1)
O(1a)$^+$	6*c*	0.179(1)	2 *x*	0.4157(7)	0.007(2)
O(2)$^+$	6*c*	0.301(1)	1/2 *x*	0.2472(9)	0.011(1)
O(3)$^+$	2*b*	2/3	1/3	0.414(1)	0.008(3)
O(3a)$^+$	2*b*	2/3	1/3	0.076(1)	0.011(4)

$^+$ refined with isotropic displacements parameters.
**M*(1) = 0.86(2) Sn, 0.14 Fe; *M*(1a) = 0.54(2) Sn, 0.46 Fe; *M*(2) = 0.161(6) Sn, 0.839 Fe; Fe(3) = 0.19(2) Fe; Fe(3a) = 0.81 Fe

Atom	U_{11}	U_{22}	U_{33}	U_{23}	U_{13}	U_{12}
Sr	0.0149(6)	U_{11}	0.019(1)	0	0	1/2 U_{11}
M(1)	0.008(2)	U_{11}	0.011(1)	0	0	1/2 U_{11}
M(1a)	0.001(2)	U_{11}	0.005(2)	0	0	1/2 U_{11}
M(2)	0.0059(4)	0.0045(5)	0.0086(5)	0.0005(4)	1/2 U_{23}	1/2 U_{22}
Fe(3)/Fe(3a)	0.006(1)	U_{11}	0.013(4)	0	0	1/2 U_{11}

Table 3. Selected distances (Å) for $SrSn_2Fe_4O_{11}$ with estimated standard deviations in parentheses.

Sr	–O(1a)	2.77(1)	3 ×
	–O(1)	2.83(1)	6 ×
	–O(2)	2.9817(4)	6 ×
M(1)	–*M*(1a)	2.905(1)	1 ×
	–O(1)	1.97(1)	3 ×
	–O(2)	2.096(9)	3 ×
M(1a)	–*M*(1)	2.905(1)	1 ×
	–O(1a)	2.01(1)	3 ×
	–O(2)	2.157(9)	3 ×
M(2)	–O(3a)	1.999(9)	1 ×
	–O(1)	2.010(9)	2 ×
	–O(1a)	2.013(8)	2 ×
	–O(3)	2.08(1)	1 ×
	–*M*(2)	2.971(3)	2 ×
	–*M*(2)	2.983(3)	1 ×
Fe(3)	–Fe(3a)	0.54(3)	1 ×
	–O(2)	1.914(9)	3 ×
	–O(3a)	1.99(4)	1 ×
Fe(3a)	–Fe(3)	0.54(3)	1 ×
	–O(2)	1.895(6)	3 ×
	–O(3)	2.07(2)	1 ×

Figure Captions

Fig. 1. Crystal structure of $SrSn_2Fe_4O_{11}$. The unit cell shown is extended by the oxide coordination of the metal atoms. Dark ellipsoids represent Sr. Small, dark ellipsoids represent mixed occupation by Fe/Sn in octahedral coordination, or Fe in tetrahedral coordination. Light spheres represent O. Atoms are depicted with displacement ellipsoids with 90 % probability.

Fig. 2. Section of the crystal structure of $SrSn_2Fe_4O_{11}$. Sr is coordinated by twelve oxygen atoms that define a nearly ideal anti-cuboctahedron. Face-sharing octahedral sites have mixed occupation by Sn/Fe atoms with different ratios (M(1) by 86 % Sn, M(1a) by 54 % Sn). Face-sharing tetrahedra are occupied to a different extent: Fe(3) to 19 %, Fe(3a) to 81 %, which corresponds to a shift of the Fe(3a) atoms by about 0.2 Å off the ideal center position along [001] in the trigonal bipyramidal void. Atoms are depicted with displacement ellipsoids with 90 % probability.

Fig. 3. Temperature dependence of the FC DC magnetic susceptibility $\chi(T)$ of a $SrSn_2Fe_4O_{11}$ single crystal for $\boldsymbol{H} \perp \mathbf{c}$ and $\boldsymbol{H} \parallel \mathbf{c}$ in applied magnetic field $\mu_o H$ = 0.1 T. Arrows designate the high-temperature onset of long-range magnetic order, and the much lower onset temperature of spin glass order at T_f = 35.8 K.

Fig. 4. Coercive field $H_{C\perp}$ for DC field applied perpendicular to the ***c*-**axis, versus temperature T for a $SrSn_2Fe_4O_{11}$ single crystal. The dashed line is a fit to **Eq. 1** (see text for details) using parameters H_{CO} = 5.06 Oe, T_1 = 4.60 K, H_{C1} = 391 Oe, T_2 = 37.9 K, and H_{C2} = 58.1 Oe. **Inset:** The low-temperature dependence of the ZFC and FC dc magnetic moment of a $SrSn_2Fe_4O_{11}$ single crystal for applied field $\boldsymbol{H}$ parallel and perpendicular to the ***c*-**axis. Arrow designates the spin glass transition temperature T_f = 35.8 K.

Fig. 5. Magnetic moment *m* vs. applied field $\boldsymbol{H} \perp \mathbf{c}$ for temperatures $T = 300$ K (solid line) and $T = 4.5$ K (dashed lines) for a $SrSn_2Fe_4O_{11}$ single crystal. Note the lack of saturation for $T = 4.5$ K, and the very small hysteresis for dc applied field swept back and forth between ± 5 T. Note also the very similar behavior of these data and those of **Fig. 6** for $\boldsymbol{H} \parallel \boldsymbol{c}$.

Fig. 6. Magnetic moment *m* vs. applied field $\boldsymbol{H} \parallel \mathbf{c}$ for temperatures $T = 300$ K (solid line) and $T = 4.5$ K (dashed lines) for a $SrSn_2Fe_4O_{11}$ single crystal. Note the lack of saturation for $T = 4.5$ K, and the very small hysteresis for dc applied field swept back and forth between ± 5 T. Note also the very similar behavior of these data and those of **Fig. 5** for $\boldsymbol{H} \perp \boldsymbol{c}$.

Fig. 7. Temperature and frequency dependences of the **a)** real, χ', and **b)** imaginary, χ'', parts of the ac susceptibility of a $SrSn_2Fe_4O_{11}$ single crystal for applied ac magnetic field $\boldsymbol{h} \perp \mathbf{c}$, with RMS magnitude 5.0 Oe. The vertical dashed line in **a)** indicates the frequency-independent temperature T_k of a kink in χ', which corresponds well with the proposed freezing temperature, $T_f = 35.8$ K (see **Fig. 3**).

Fig. 8. Dependence of the anomaly temperatures T_k, T_p and T_i on the ac measuring frequency *f* from the ac moment data of **Fig. 7**.

Fig. 9. Logarithm (base-10) of the measuring frequency log *f* versus the inverse of the peak temperature in $\chi''(T)$, $1/T_p$ (see **Fig. 7b**), for a $SrSn_2Fe_4O_{11}$ single crystal. The solid line is a fit of the data to the Arrhenius law (**Eq. 3**) with $E_a/k_B = 138$ K and $\log(f_0) = 6.7134$, corresponding to $f_0 = 5.169 \times 10^6$ Hz. Note the appreciable deviations from the fit below 20 K.

Fig. 10. Frequency dependence of the imaginary part of the ac susceptibility, χ"(*f*), at different temperatures (see online for color key).

Fig. 11. Time dependence of the magnetic moment *m* of a $SrSn_2Fe_4O_{11}$ single crystal at $T = 25$ K (see text for experimental protocol). Dotted line corresponds to power law fit (**Eq. 6**) with parameters: $M_0 = 6.8 \times 10^{-3}$ emu/mol, $\gamma = 0.18$. Dashed line corresponds to stretched exponential fit (**Eq. 4**) with parameters: $M_0 = 2.6 \times 10^{-2}$ emu/mol, $\tau = 255$ s, $n = 0.1$. Solid line corresponds to **Eq. 7** with parameters $M_0 = 6.8 \times 10^{-3}$ emu/mol, $\gamma = 0.18$, $M_1 = 2.6 \times 10^{-2}$ emu/mol, $\tau = 255$ s, and $n = 0.1$.

Fig. 12. Plot of the Kubelka-Munk function (α/S) against energy. The absorption edge energies are derived from the individual intersection point of the base lines drawn along the energy axis and the extrapolated lines of the linear parts of the threshold.

Figures

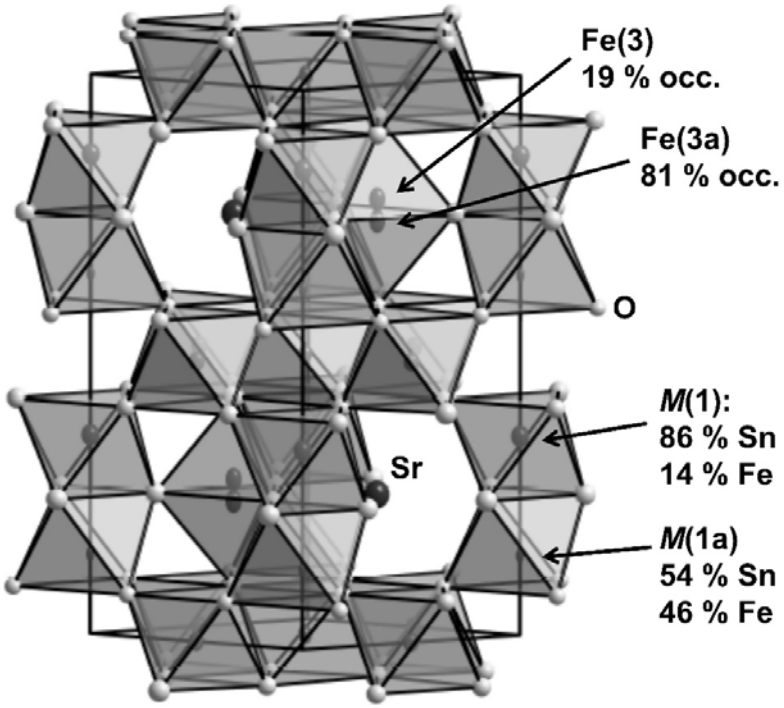

Fig. 1. Crystal structure of $SrSn_2Fe_4O_{11}$. The unit cell shown is extended by the oxide coordination of the metal atoms. Dark ellipsoids represent Sr. Small, dark ellipsoids represent mixed occupation by Fe/Sn in octahedral coordination, or Fe in tetrahedral coordination. Light spheres represent O. Atoms are depicted with displacement ellipsoids with 90 % probability.

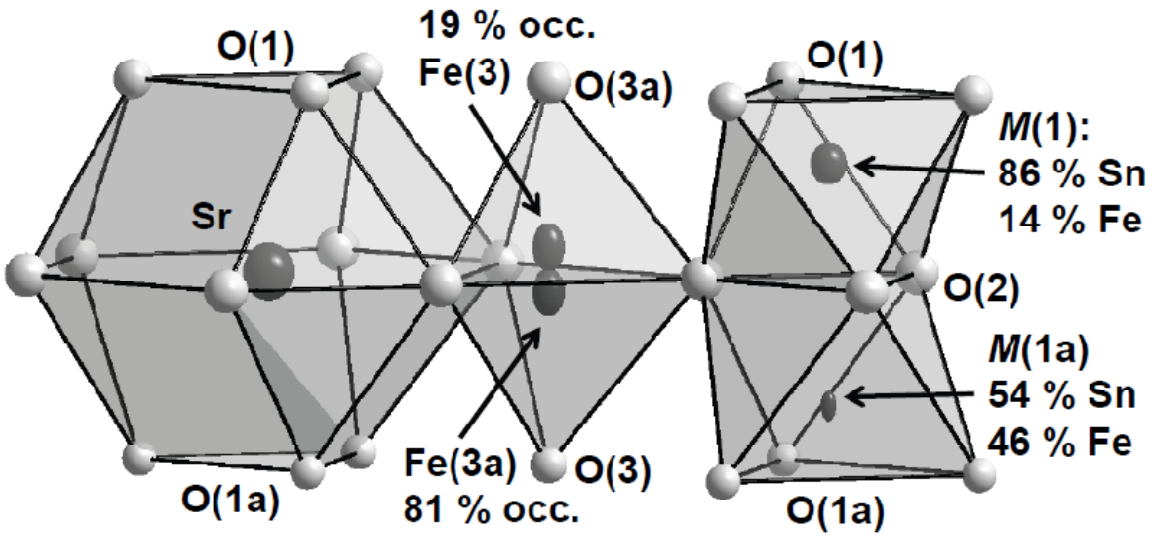

Fig. 2. Section of the crystal structure of $SrSn_2Fe_4O_{11}$. Sr is coordinated by twelve oxygen atoms that define a nearly ideal anti-cuboctahedron. Face-sharing octahedral sites have mixed occupation by Sn/Fe atoms with different ratios (*M*(1) by 86 % Sn, *M*(1a) by 54 % Sn). Face-sharing tetrahedra are occupied to a different extent: Fe(3) to 19 %, Fe(3a) to 81 %, which corresponds to a shift of the Fe(3a) atoms by about 0.2 Å off the ideal center position along [001] in the trigonal bipyramidal void. Atoms are depicted with displacement ellipsoids with 90 % probability.

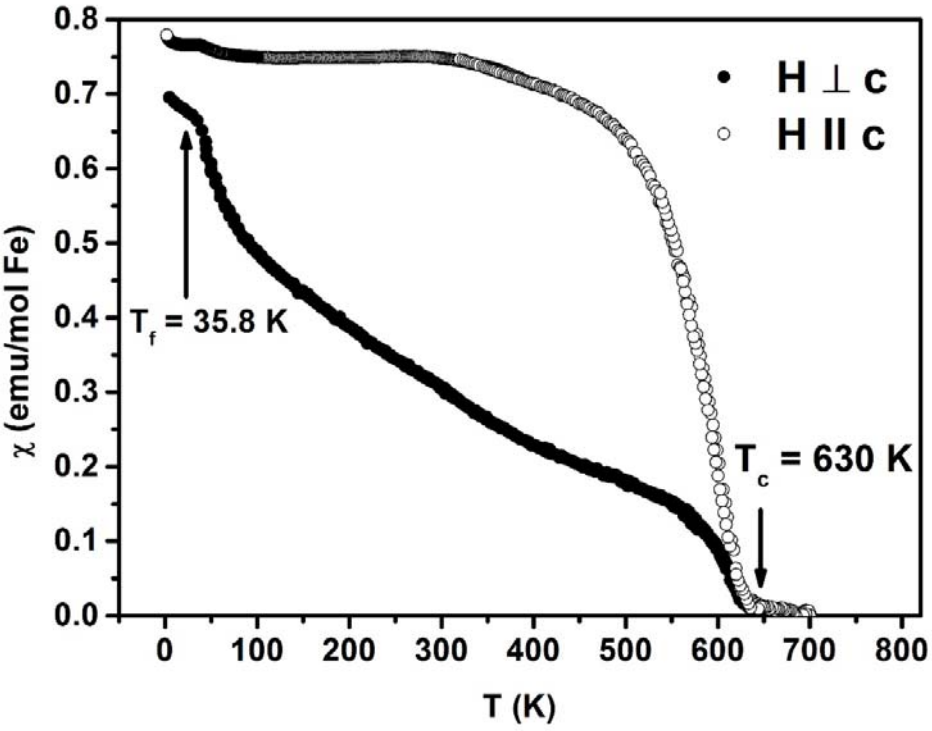

Fig. 3. Temperature dependence of the FC DC magnetic susceptibility $\chi(T)$ of a $SrSn_2Fe_4O_{11}$ single crystal for $\boldsymbol{H} \perp \mathbf{c}$ and $\boldsymbol{H} \parallel \mathbf{c}$ in applied magnetic field $\mu_o H = 0.1$ T. Arrows designate the high-temperature onset of long-range magnetic order, and the much lower onset temperature of spin glass order at $T_f = 35.8$ K.

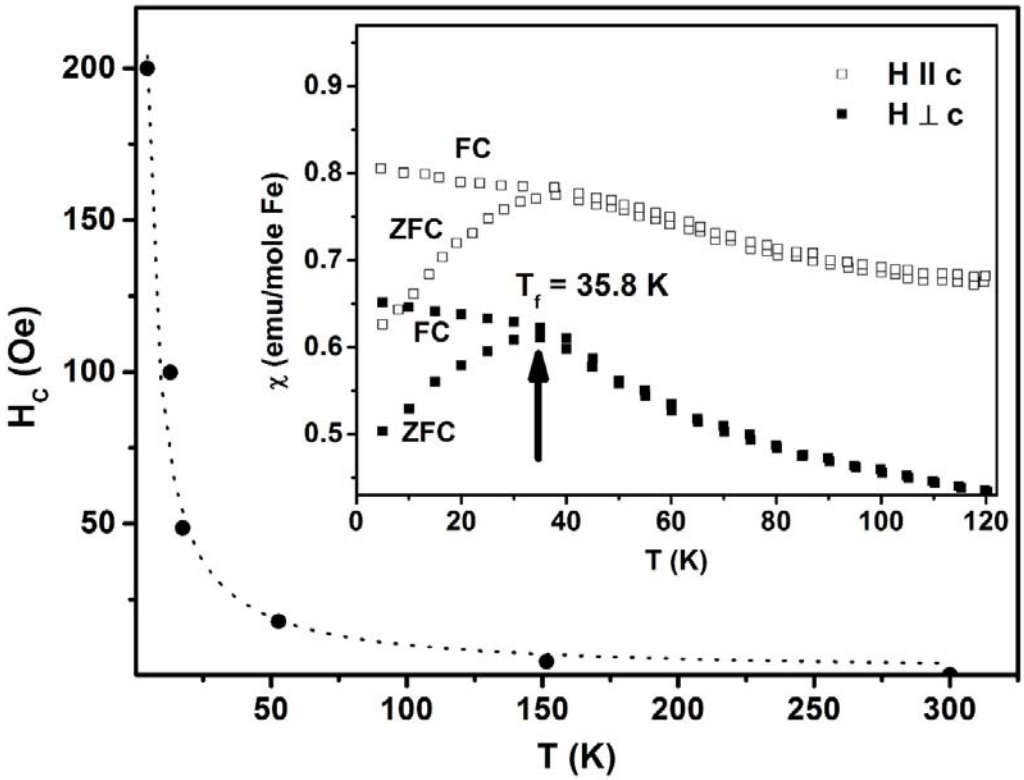

Fig. 4. Coercive field $H_{C\perp}$ for DC field applied perpendicular to the ***c***-axis, versus temperature *T* for a $SrSn_2Fe_4O_{11}$ single crystal. The dashed line is a fit to **Eq. 1** (see text for details) using parameters H_{CO} = 5.06 Oe, T_1 = 4.60 K, H_{C1} = 391 Oe, T_2 = 37.9 K, and H_{C2} = 58.1 Oe. **Inset:** The low-temperature dependence of the ZFC and FC dc magnetic moment of a $SrSn_2Fe_4O_{11}$ single crystal for applied field ***H*** parallel and perpendicular to the ***c***-axis. Arrow designates the spin glass transition temperature T_f = 35.8 K.

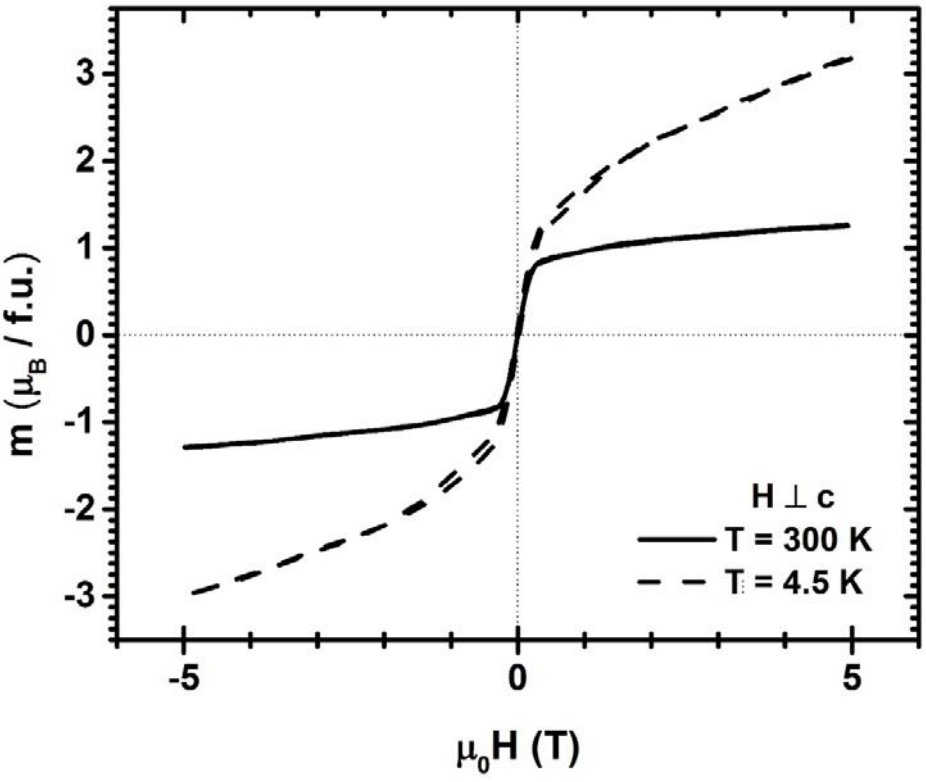

Fig. 5. Magnetic moment *m* vs. applied field ***H*⊥ c** for temperatures *T* = 300 K (solid line) and *T* = 4.5 K (dashed lines) for a $SrSn_2Fe_4O_{11}$ single crystal. Note the lack of saturation for *T* = 4.5 K, and the very small hysteresis for dc applied field swept back and forth between ± 5 T. Note also the very similar behavior of these data and those of **Fig. 6** for ***H* || *c***.

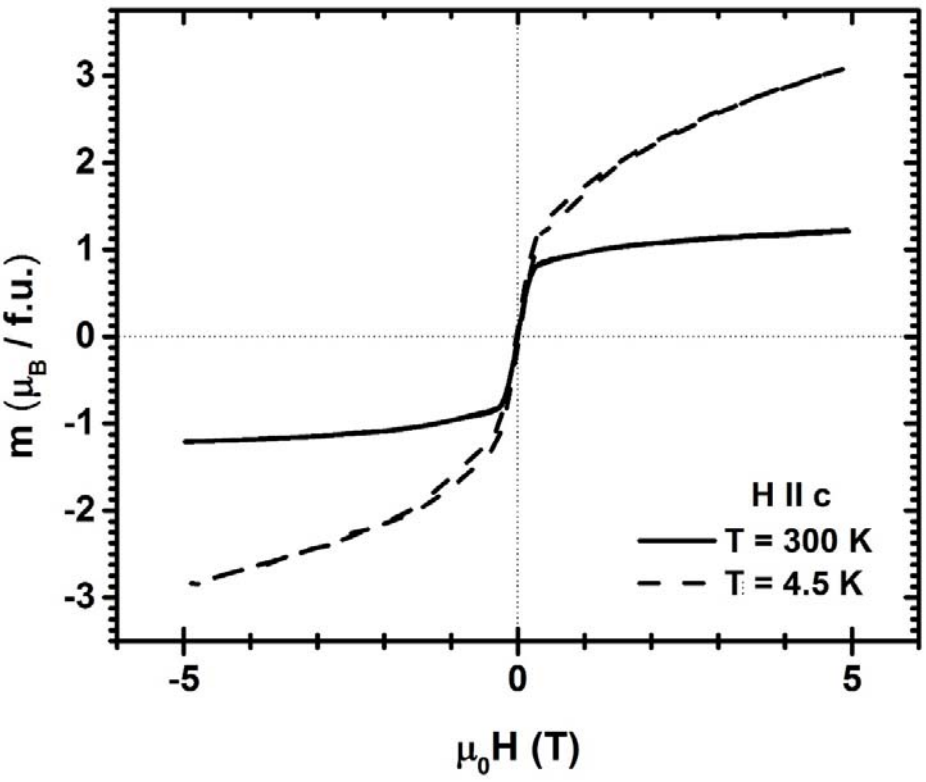

Fig. 6. Magnetic moment *m* vs. applied field ***H*** || **c** for temperatures *T* = 300 K (solid line) and *T* = 4.5 K (dashed lines) for a $SrSn_2Fe_4O_{11}$ single crystal. Note the lack of saturation for *T* = 4.5 K, and the very small hysteresis for dc applied field swept back and forth between ± 5 T. Note also the very similar behavior of these data and those of **Fig. 5** for ***H*** ⊥ ***c***.

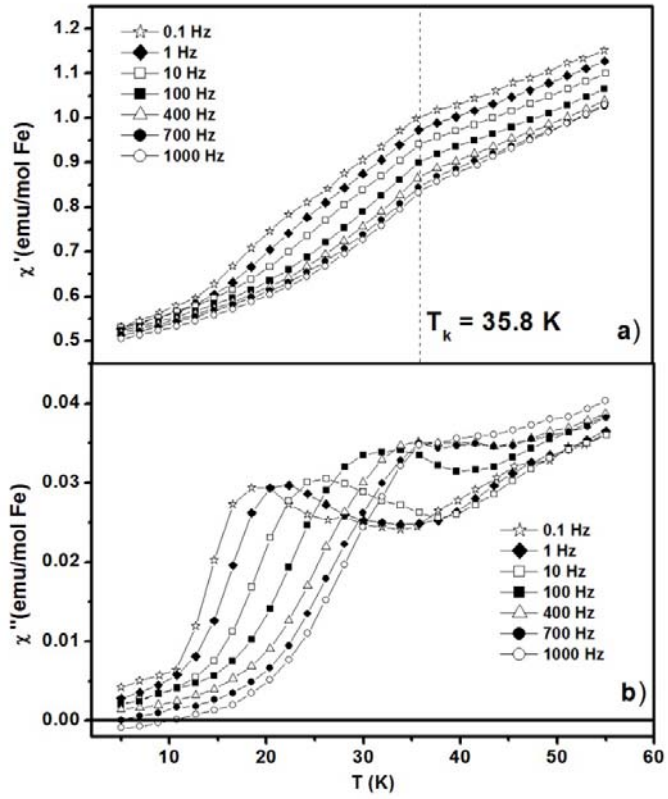

Fig. 7. Temperature and frequency dependences of the **a)** real, χ', and **b)** imaginary, χ'', parts of the ac susceptibility of a $SrSn_2Fe_4O_{11}$ single crystal for applied ac magnetic field $\boldsymbol{h} \perp \mathbf{c}$, with RMS magnitude 5.0 Oe. The vertical dashed line in **a)** indicates the frequency-independent temperature T_k of a kink in χ', which corresponds well with the proposed freezing temperature, $T_f = 35.8$ K (see **Fig. 3**).

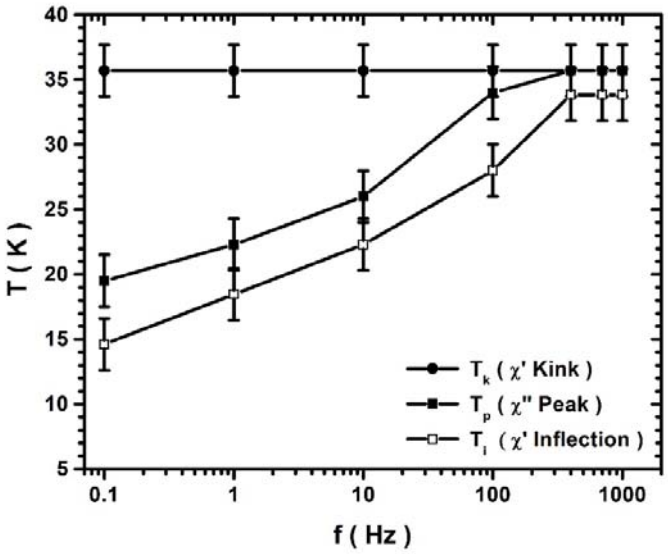

Fig. 8. Dependence of the anomaly temperatures T_k, T_p and T_i on the ac measuring frequency *f* from the ac moment data of **Fig. 7**.

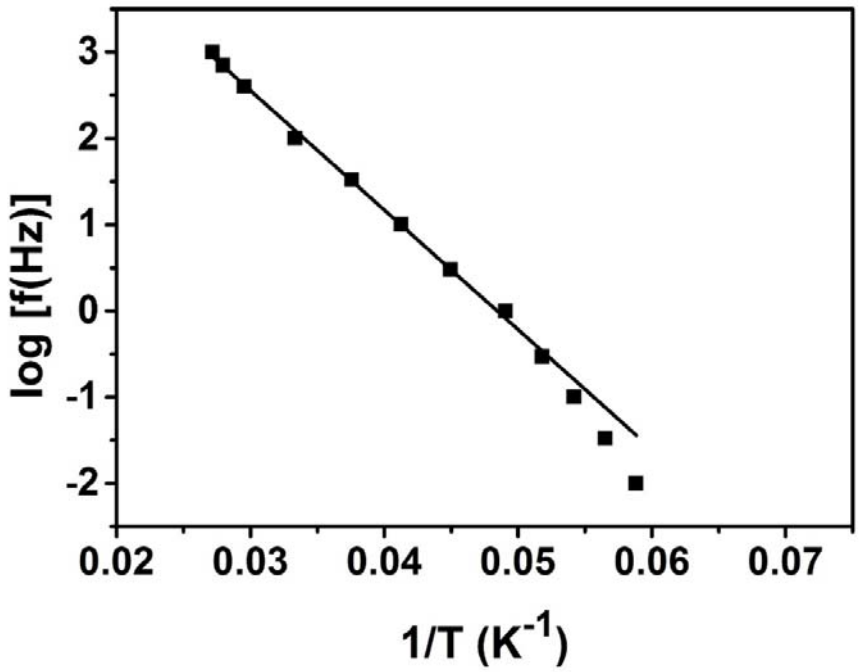

Fig. 9. Logarithm (base-10) of the measuring frequency log f versus the inverse of the peak temperature in $\chi''(T)$, $1/T_p$ (see **Fig. 7b**), for a $SrSn_2Fe_4O_{11}$ single crystal. The solid line is a fit of the data to the Arrhenius law (**Eq. 3**) with E_a/k_B = 138 K and $\log(f_0) = 6.7134$, corresponding to $f_0 = 5.169 \times 10^6$ Hz. Note the appreciable deviations from the fit below 20 K.

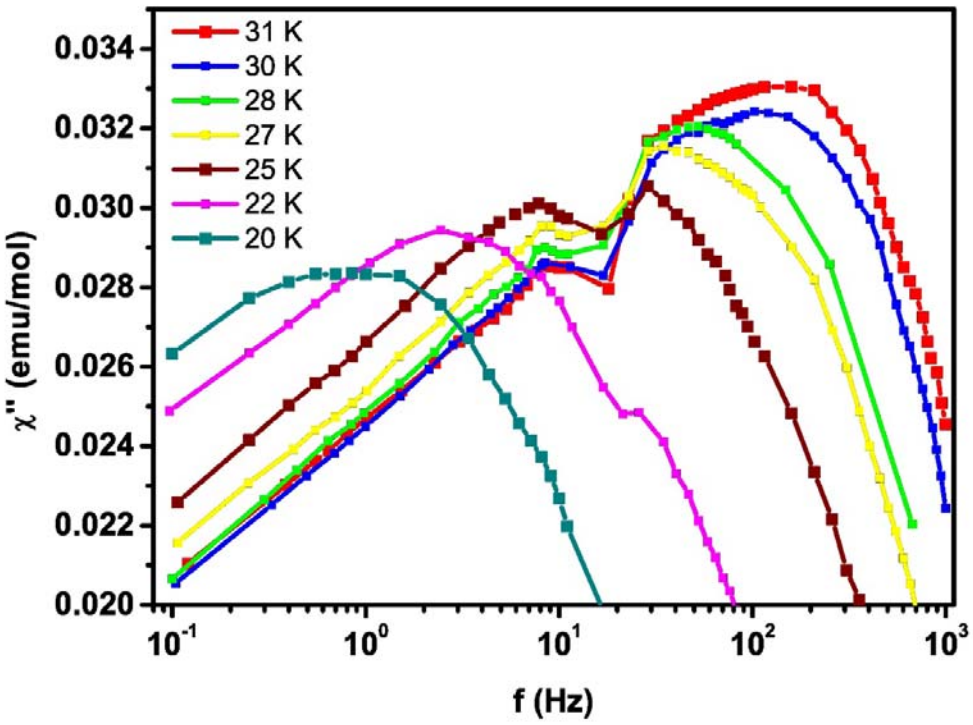

Fig. 10. Frequency dependence of the imaginary part of the ac susceptibility, χ”(*f*), at different temperatures (see online for color key).

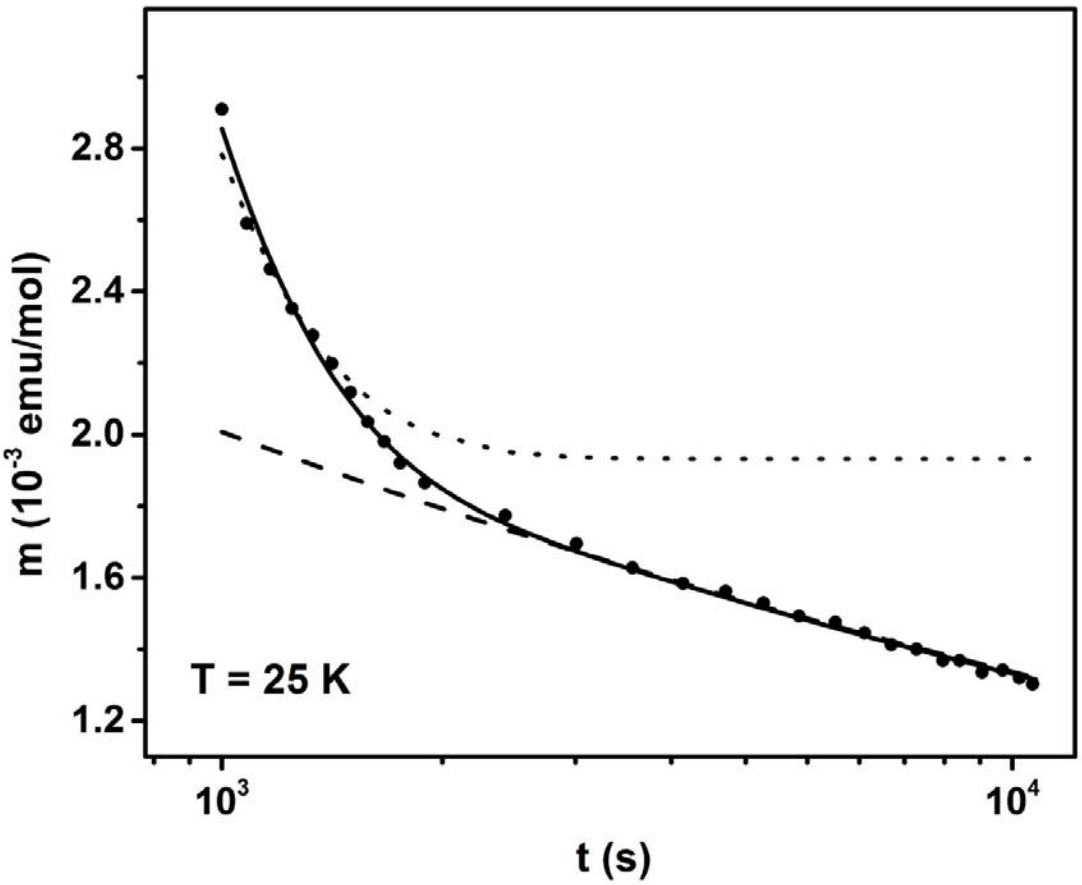

Fig. 11. Time dependence of the magnetic moment *m* of a $SrSn_2Fe_4O_{11}$ single crystal at $T = 25$ K (see text for experimental protocol). Dotted line corresponds to power law fit (**Eq. 6**) with parameters: $M_0 = 6.8 \times 10^{-3}$ emu/mol, $\gamma = 0.18$. Dashed line corresponds to stretched exponential fit (**Eq. 4**) with parameters: $M_0 = 2.6 \times 10^{-2}$ emu/mol, $\tau = 255$ s, $n = 0.1$. Solid line corresponds to **Eq. 7** with parameters $M_0 = 6.8 \times 10^{-3}$ emu/mol, $\gamma = 0.18$, $M_1 = 2.6 \times 10^{-2}$ emu/mol, $\tau = 255$ s, and $n = 0.1$.

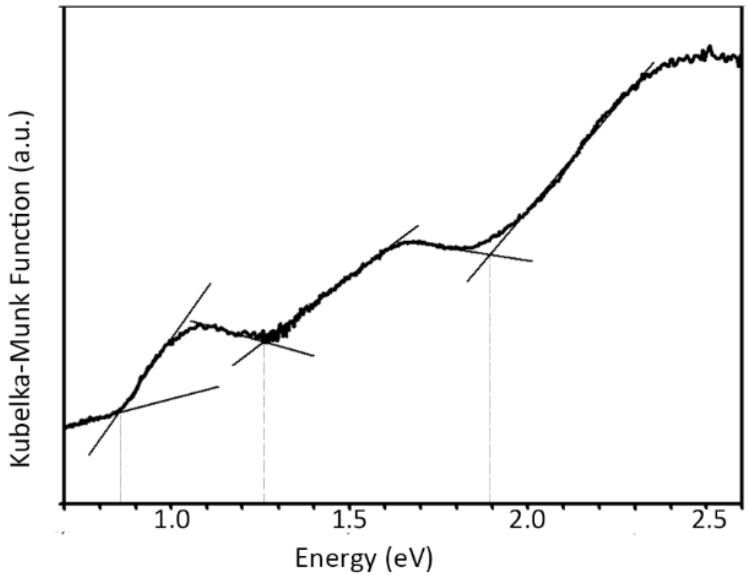

Fig. 12. Plot of the Kubelka-Munk function (α/S) against energy. The absorption edge energies are derived from the individual intersection point of the base lines drawn along the energy axis and the extrapolated lines of the linear parts of the threshold.